Nature Communications

https://doi.org/10.1038/s41467-025-67985-x

Article in Press

Surface halogenation engineering for reversible silicon-based solid-state batteries

Received: 26 May 2025

Accepted: 15 December 2025

Cite this article as: Li, H., Li, Y., Hu, G. *et al.* Surface halogenation engineering for reversible silicon-based solid-state batteries. *Nat Commun* (2025). https://doi.org/10.1038/s41467-025-67985-x

Haosheng Li, Yaru Li, Guantai Hu, Ying Li, Caijin Xiao, Liang Zhao, Huiqin Huang, Haochang Zhang, Wei Xia & Ning Lin

Surface Halogenation Engineering for Reversible Silicon-Based Solid-State Batteries

Haosheng Li[1,2], Yaru Li[1], Guantai Hu[2], Ying Li[2], Caijin Xiao[3], Liang Zhao[3], Huiqin Huang[4], Haochang Zhang[2], Wei Xia[2,*], Ning Lin[1,*]

[1]Yongjiang Laboratory, Ningbo, Zhejiang 315201, China

[2]Eastern Institute for Advanced Study, Eastern Institute of Technology, Ningbo, Zhejiang 315200, China

[3]Department of Nuclear Physics, China Institute of Atomic Energy, Beijing 102413, China

[4]School of Materials Science and Engineering, Zhejiang University, Hangzhou, Zhejiang 310027, China

*Corresponding authors: W. X. (wxia@eitech.edu.cn) and N. L. (ning-lin@ylab.ac.cn)

Abstract

Silicon-based solid-state batteries are promising next-generation high-energy-density technologies. However, poor (electro)chemical compatibility between silicon negative electrodes and solid electrolytes (e.g., Li_6PS_5Cl) plus sluggish interfacial kinetics severely limits their reversibility and Coulombic efficiency. Here, we propose a surface halogenation strategy that transforms the native amorphous SiO_2 passivation layer on silicon particles into a functional Al(Si)OCl composite surface via controlled reaction with $AlCl_3$. This artificial interphase reconciles interfacial incompatibility and enables fast ionic/electronic transport, suppressing irreversible lithium loss. The optimized negative electrode achieves a high initial Coulombic efficiency of 94.3% in half-cells and 85.6% initial Coulombic efficiency (86.6% with pre-lithiation) in full cells paired with $LiNi_{0.88}Co_{0.09}Mn_{0.03}O_2$. Enhanced reversibility further delivers long-term cyclability. The optimized negative electrode delivers 86% capacity retention and 99.998% average Coulombic efficiency over 200 cycles. Even at high-loading (>10 mAh cm^{-2}, and no adhesives/conductive carbon/electrolyte), it retains 72% capacity after 500 cycles. The full cells maintain 80% capacity after 200 cycles at 1C, with an average Coulombic efficiency exceeding 99.95%. The versatility of this halogenation strategy underscores halide chemistry's broad potential in advancing high-performance, reversible silicon-based solid-state batteries.

Keywords: Si negative electrode; solid-state batteries; Coulombic efficiency; halide; interface

Introduction

All solid-state batteries (SSBs) are recognized as a leading next-generation electrochemical energy storage technologies due to their superior energy density and inherent safety advantages[1,2]. Silicon (Si) negative electrodes are particularly promising for SSBs due to their exceptional theoretical specific capacity of 3579 mAh g^{-1}, which approaches that of metallic lithium (Li) negative electrodes (3860 mAh g^{-1})[3,4]. Moreover, Si negative electrodes demonstrate an intrinsic resistance to Li dendrite formation owing to their moderate operating potential (~0.1–0.5 V vs. Li^+/Li), and exhibit higher critical current densities compared to lithium-indium (Li-In) alloys[3,5]. The inherent safety advantages and favorable electrochemical performance highlight the promising development potential of Si-based SSBs.

However, Si-based SSBs currently face challenges in suboptimal electrochemical reversibility and insufficient Coulombic efficiency, including initial Coulombic efficiency (ICE) and cycling Coulombic efficiency (CE), significantly limiting their practical capacity utilization and energy density[3,6]. The typical ICE ranges between 78–90% in half-cell configurations employing Li_6PS_5Cl (LPSC) solid electrolytes (SEs) while only approximately 80% could be achieved in full cells paired with $LiNi_{1-x-y}Co_xMn_yO_2$ positive electrodes[7-12]. Research indicates that irreversible capacity loss during initial charge-discharge cycles includes Li consumption for solid electrolyte interphase (SEI) formation (C-Li) and kinetically trapped Li (K-Li), accounting for approximately 12% and 11% of the total capacity, respectively[5]. C-Li stems from the poor (electro)chemical compatibility at the Si|LPSC interface[3,13]. K-Li is primarily caused by inadequate bulk and interfacial ion/electron transport kinetics, resulting in the formation of insulating dead Li-Si alloy[14,15](Fig. 1a). Although it has been suggested that SEI could be “frozen” at the interface once it was formed in SSBs, potentially ensuring cycling stability[5,13], subsequent experimental investigations revealed continuous SEI growth and void formation at the 2-dimensional Si|LPSC interface, leading to increased impedance and suboptimal cycling CE (<99% during the first 50 cycles)[3,16].

To tackle these issues, pre-lithiation and Li-Si alloys incorporation strategies are the most straightforward approaches for compensating irreversible Li loss[4,6,14]. For example, a direct Li metal powder pre-lithiation process has been proposed to achieve 85.2% capacity retention after 200 cycles

and an average CE of 99.6%[17]. Similarly, LiSi alloy negative electrode exhibits an enhanced ICE from 75.4% to 80.8% with an average CE of 99.9% when paired with NCM811 positive electrode[6]. However, excessive Li usage raises safety concerns (such as soft short circuits), while the highly active Li-Si alloys would exacerbate interfacial side reactions[4,18,19].

In addition, other major research efforts have focused on stabilizing SEI film. A poly(vinylidene fluoride-co-hexafluoropropylene) (PVDF-HFP)/$Li_{1.3}Al_{0.3}Ti_{1.7}(PO_4)_3$ SE is developed to construct a stable LiF-rich SEI layer, achieving 89.6% ICE for Si negative electrodes[17]. $LiBH_4$-LiI (LBHI) SEs demonstrate electrochemical compatibility with Si negative electrodes, effectively suppressing continuous SEI formation. Although the LBHI-based half-cell could deliver an high ICE of 96.2%, it was achieved under a high temperature 60°C and the cycling performance was limited by compromised ionic transport kinetics due to the substitution of LPSC with LBHI resulting in an insufficient average CE of 99.34%[13].

Despite these advancements, cycling CE remains below the critical 99.98% threshold (calculated for 80% capacity retention over 1000 cycles[20]). Thus, the ICE of the full cell with commercial NCM-based positive electrodes is still suboptimal, typically below 85%. In this regard, we were inspired by halogen chemistry, as the potential of both halide modifications and halide-based SEs in stabilizing interfaces[21-23]. Capitalizing on the thermodynamic reactivity between the SiO_2 and halide salts such as $AlCl_3$[24,25], a surface halogenation strategy is developed through a simple mixing and heating process of $AlCl_3$ and Si (denoted as Si@$AlCl_3$) (Fig. 1b). It is revealed that the inert amorphous SiO_2 (a-SiO_2) layer on the Si surface can be converted to Al(Si)OCl. This transformation endows the Si@$AlCl_3$|LPSC interface with enhanced chemical/electrochemical stability, significantly improving ion/electron transport kinetics. This optimization could not only effectively suppress C-Li induced by interfacial side reactions, but also mitigate K-Li, thereby breaking the reversibility barrier. The modified system achieves an ICE of 94.3% in half cell and 85.6% in full cell with commercial $LiNi_{0.88}Co_{0.09}Mn_{0.03}O_2$ (NCM) positive electrodes at 25 °C, further boosting a high ICE of 86.6% with pre-lithiation. The improved reversibility improves cycling stability. The Si@$AlCl_3$ negative electrode exhibits a capacity retention increase from 14% (for Si) to 86% after 200 cycles at 3C, with average

CE improving from 99.4% to 99.998%. At high loading (>10 mAh cm^{-2}), the Si@$AlCl_3$ negative electrode without any adhesives, conductive carbon or SE maintains 72% capacity retention after 500 cycles with a current density of 5.1 mA cm^{-2}. The assembled NCM-based SSBs show 80% capacity retention after 200 cycles at 200 mA g^{-1}. Furthermore, the universal applicability of halide salts in enhancing reversibility and capacity of Si negative electrode was validated, highlighting the significant potential of the surface halogenation engineering for Si-based SSBs.

Results and discussion

$AlCl_3$-Mediated Surface Halogenation Modification

$AlCl_3$ was selected as the primary research subject owing to its suitably low boiling points among halide salts, as well as its spontaneous reactivity with SiO_2 (Fig. S1 and Table S1). As depicted in Figure 2a,b, pre-experimental validation confirms the thermodynamically driven phase transformation process, where a-SiO_2 reacts with $AlCl_3$ to form AlOCl and $SiCl_4$ (SA), as evidenced by X-ray diffraction (XRD), Raman spectroscopy, and X-ray photoelectron spectroscopy (XPS) analyses[26,27] (Fig. S2-S4; the detail is discussed in the Supplementary information). The chemical stability of SA to Li has also been experimentally verified (Fig. S5, the detail is provided in the Supplementary information). Consequently, we conducted the halogenation reaction by sealing a mixture of $AlCl_3$ and micron-sized Si particles and heating it at 180°C. Electrochemical evaluation of Si negative electrodes with varying $AlCl_3$ mass fractions reveals a non-monotonic relationship between ICE and $AlCl_3$ content, peaking at 10% incorporation (Fig. S6 and Table S2). Therefore, the optimal 10% $AlCl_3$-incorporated system (designated as Si@$AlCl_3$) was selected for subsequent investigations.

Scanning electron microscopy (SEM) imaging coupled with energy dispersive spectroscopy (EDS) elemental mapping confirms the presence and characteristic distribution of Si, Al, and Cl elements throughout both Si@$AlCl_3$ particles (Fig. S7) and the corresponding electrodes (Fig. S8-S9), showing relatively consistent elemental dispersion. The XRD analysis reveals the main phase of crystalline Si with the emergence of a weak $AlCl_3$ signal at 31° compared to pristine Si (Fig. S10). Raman spectroscopy demonstrates a new high-wavenumber peak alongside the Si-Si vibrational peak,

consistent with SiCl(O) observed in pre-experiments (Fig. 2c and Fig. S2). The XPS analysis reveals a red-shift in the Si 2*p* and O 1*s* peaks for Si@$AlCl_3$ particles compared to pure Si, which is also consistent with the shift characteristic of SiCl(O). Specifically, the O 1*s* peak shifts from 532.4 eV (SiO_2)[28] to a lower binding energy of 531.7 eV, while the Al 2*p* peak of Si@$AlCl_3$ displays a slight decrease in binding energy to 74.7 eV relative to pure $AlCl_3$ (75.1 eV). This aligns with reported values for AlOCl[29,30]. The Cl 2*p* peaks of Si@$AlCl_3$ at 199.5 and 201 eV exhibits binding energies consistent with pure $AlCl_3$ (Fig. 2d-f, Fig. S11 and Fig. S12a-c). Furthermore, HRTEM imaging reveals significant surface differences between pristine Si and Si@$AlCl_3$. The initial Si particles display an a-SiO_2 surface layer of 5-10 nm (Fig. 2g, h). After reacting with $AlCl_3$, a crystalline layer exhibiting the triclinic $AlCl_3$ and AlOCl interplanar spacing characteristic is generated, and a-SiO_2 is completely eliminated on Si@$AlCl_3$ surface (Fig. 2i and Fig. S13). EDS elemental mapping and line scan profiles further confirms the halogenated modification layer (Fig. 2j and Fig. S14). Based on the above experimental observations, we propose a mechanistic pathway wherein $AlCl_3$, functioning as a Lewis acid catalyst, facilitates the chemical modification of the native SiO_2 layer[31], consequently generating Al(Si)OCl and residual $AlCl_3$ (SA).

Study of irreversible Li loss

As illustrated in Fig. 3a, the reversibility of Si and Si@$AlCl_3$ was explored through electrochemical measurements at 25 °C. The Si@$AlCl_3$ half-cell demonstrates an enhanced ICE of 94.3%, compared to 88.4% for the pure Si negative electrode. Additionally, the specific charge capacity of the Si active material improves from 2924 mAh g^{-1} to 3324.6 mAh g^{-1} (Fig. 3c). Correspondingly, ICE of the full cell paired with a NCM positive electrode increases from around 79.2% to a maximum of 85.6% (Fig. 3b, Fig. S15 and Table S3). It is demonstrated that the Si@$AlCl_3$ negative electrode exhibits enhanced reversibility compared with pure Si negative electrode.

The reversibility in Si-based negative electrodes is closely associated with the mitigation of irreversible Li loss. Neutron depth profiling (NDP), a non-destructive neutron-based characterization technique, is particularly suited for studying Li concentration spatial distribution due to its high

sensitivity to Li[32]. Therefore, NDP (Fig. 3d and Fig. S16) coupled with gas chromatography (GC) (Fig. 3e) was employed to analyze Si@$AlCl_3$ and pristine Si negative electrodes during the initial (de)lithiation process. The results reveal a significant reduction in irreversible Li loss in Si@$AlCl_3$ compared to pristine Si negative electrodes. The specific distribution of irreversible Li is characterized as follows: (1) A distinct concentration gradient of residual Li is observed within the Si-based negative electrode layer, exhibiting a gradual decrease from the Si|SE interface towards the bulk region. The interfacial region demonstrates higher Li content (corresponding to C-Li for SEI formation), accounting for the majority of irreversible Li, while the bulk region displays lower Li content (corresponding to K-Li), representing a minor fraction of irreversible Li (Fig. 3f). (2) In Si@$AlCl_3$ negative electrodes, the Li concentration near the interface is substantially reduced compared to pristine Si negative electrodes, indicating suppressed C-Li (decreased from 9.9% to 7.5%). (3) The bulk Li content in Si@$AlCl_3$ negative electrodes exhibits a remarkable decrease (from 1.5% to 0.1%), signifying reduced K-Li. In addition, a constant-current/constant-voltage (CC-CV) charging protocol was implemented for the Si-based negative electrode. Comparative results reveals that the CV process effectively activates residual Li localized near the SEI within Si-based negative electrode, thereby boosting 96.1% ICE for Si@$AlCl_3$ (Fig. S17-S19).

Furthermore, the irreversible Li loss was investigated following multiple charge-discharge cycles (Fig. 3g-j). After 50 cycles, a prominent signal of kinetically trapped Li_xSi is observed at 54.5 eV for the Si negative electrode[33], while no such signal is detected for the Si@$AlCl_3$ negative electrode, indicating superior cycling reversibility of the latter. Notably, elemental Al signal appears at 72.8 eV in Al 2*p* spectra and LiCl signals at 198.4 eV and 200 eV in Cl 2*p* spectra, attributed to the reduction of lithiated $AlCl_3$. In contrast, the Al 2*p* (~75 eV) and Cl 2*p* signatures corresponding to AlOCl remains stable (Fig. S20a-d). Further analysis of the GCD profiles and CV curves confirms negligible capacity contributions from SA and $AlCl_3$ (Fig. S21). These results demonstrate that $AlCl_3$ exhibits weak electrochemical reactivity during cycling, as evidenced by the absence of Al metal signal in the XPS spectra of Si@$AlCl_3$ after 5 cycles, with the Al 2*p* and Cl 2*p* binding energies consistent with reported values for AlOCl-LiCl[30] (Fig. S22). The LiCl and Al generated after multiple cycles can serve as components of

the SEI, effectively mitigating the reduction of LPSC[22]. More importantly, AlOCl maintains relatively electrochemically stable throughout cycling, which plays a crucial role in ensuring the reversibility of Si-based negative electrodes in subsequent cycles.

Electrochemical/chemical compatibility of Si-based negative electrode with LPSC

Given that the C-Li caused by interfacial side reactions make the majority contribution to irreversible Li loss, the chemical compatibility was first investigated to elucidate the underlying mechanisms by which surface halogenation enhances electrochemical reversibility and improves the ICE. A physical mixing approach was employed, where Si-based particles were uniformly mixed with LPSC powder with a 2:1 mass ratio to obtain Si+LPSC and Si@$AlCl_3$+LPSC, respectively (Fig. 4a). XPS spectra reveals that pure Si particles exhibit poor chemical stability with LPSC powder (Fig. 4b and Fig. S23a). The Si 2*p* binding energy for Si+LPSC is observed at 98.7 and 99.4 eV, indicating a redshift compared to the binding energies of pure Si at 99.0 and 99.6 eV. The S 2*p* binding energy indicates the presence of minor Li_2S signal peaks at 162.1 and 163.5 eV, along with oxidized states at 167.1 and 168.2 eV[34]. Additionally, the P 2*p* binding energy indicates the presence of Li_xP signal peaks at 128.7 and 129.5 eV, along with oxidized states at 133.5 and 134.6 eV[35]. The substantial formation of oxidized states is hypothesized to result from side reactions between the surface oxide layer of Si particle and LPSC[3]. In contrast, the Si 2*p*, S 2*p*, P 2*p* and Al 2*p* binding energies for Si@$AlCl_3$+LPSC remains almost unchanged compared with pure LPSC or Si@$AlCl_3$, indicating enhanced stability (Fig. 4c and Fig. S23b). The enhancement can be attributed to AlOCl in the SA layer and potentially cycling-derived AlOCl-LiCl, which exhibit higher chemical compatibility with LPSC compared to conventional oxyhalides (e.g., $LiTaOCl_4$) (Fig. S24-S27).

Electrochemical impedance spectroscopy (EIS) analysis further reveals that the impedance of Si+LiPSCl is significantly higher than that of Si@$AlCl_3$+LiPSCl. Even worse, the impedance of Si+LPSC is gradually increasing over time, while that of Si@$AlCl_3$+LPSC slightly decreases and remains stable (Fig. 4d). The distribution of relaxation times (DRT) analysis indicates that, within the range of 10^{-5} to 10^{-4} s, the peaks corresponding to grain boundary and interfacial impedances for

Si+LiPSCl are significantly higher[36] (Fig. 4e and Fig. S28). According to equivalent circuit fitting (Fig. S29 and Table S4), the grain boundary and interfacial impedances in the mid-to-high frequency region are 5.07×10^4 Ω and 1.23×10^4 Ω, respectively, with the main contribution coming from the low-frequency region, valued at 5.55×10^5 Ω. In contrast, the observed impedances in the mid-to-high frequency region for the Si@$AlCl_3$+LPSC system are significantly lower, at only 4938 Ω and 3222 Ω. This validates that the enhanced chemical stability facilitates to form a more stable initial Si@$AlCl_3$|LPSC interface.

To further investigate the electrochemical stability of Si@$AlCl_3$ with LPSC, two half-cell configurations were assembled: Li-In|LPSC|Si@$AlCl_3$ and Li-In|LPSC|Si. EIS measurements were conducted after one charge-discharge cycle followed by a 12-hour rest period (Fig. 4f). The fitted EIS data reveals a significantly higher charge transfer resistance (R_{ct}) of 189 Ω for Li-In|LPSC|Si compared to 27 Ω for Li-In|LPSC|Si@$AlCl_3$ (Fig. 4g,h and Table S5). This substantial difference primarily stems from the formation of a large interfacial impedance (147 Ω) in addition to the bulk impedance (15 Ω) in the Li-In|LPSC|Si, whereas the Li-In|LPSC|Si@$AlCl_3$ exhibits only 5 Ω bulk impedance. SEM and EDS analysis of Si negative electrode after cycling reveals extensive pore generated at the Si|LPSC interface, along with significant accumulation of Cl element, as evidenced in Fig. 4i and Fig. S30. This phenomenon is further clearly observed in cross-sectional morphology and elemental line scans, which indicate vertical cracks within cycled Si negative electrode and notable redistribution of Si, Cl, P, and S (Fig. S31, Fig. S32a,b and Fig. S34a). XPS depth profiling confirms the formation of LiCl as a side reaction product. These findings suggest poor electrochemical stability between Si and LPSC (Fig. S33). In contrast, the Si@$AlCl_3$ negative electrode maintains a well-defined interface and element distribution with LPSC without detectable side reactions (Fig. 4j, Fig. S32c and Fig. S34b). It means that the Si negative electrode suffers from both poor chemical and electrochemical stability with LPSC, which would in turn detrimentally affect transport dynamics at the interface and bulk of the negative electrode. In contrast, the Si@$AlCl_3$ negative electrode exhibits enhanced chemical/electrochemical compatibility and interfacial stability.

Charge transport kinetics and electrochemical performance

The electrochemical kinetics were systematically investigated. As illustrated in Fig. 5a,b, Li-In|LPSC|Si@$AlCl_3$ exhibits higher rate performance compared to Li-In|LPSC|Si, delivering a specific charge capacity of 3306.3 mAh g^{-1} at 350 mA g^{-1} and maintaining 1891.2 mAh g^{-1} at 7 A g^{-1}, with 57.2% capacity retention. Notably, the system preserves high rate capability even under high mass loading conditions (>9 mAh cm^{-2}) (Fig. 5c). NCM-based full-cell with Si@$AlCl_3$ negative electrode exhibits a stable specific capacity of 124.7 mAh g^{-1} at 100 mA g^{-1}, surpassing the 56.7 mAh g^{-1} of cell with pristine Si negative electrode (Fig. S35).

The enhanced rate capability can be attributed to improved charge transfer kinetics. As evidenced by direct current polarization measurements, the electronic conductivity of pristine Si is only 1.98×10^{-7} S cm^{-1}, whereas Si@$AlCl_3$ exhibits an over 40-fold improvement, reaching 7.93×10^{-6} S cm^{-1} (Fig. 5d-f and Fig. S36). This enhancement in electronic conductivity can be attributed to the SA layer, which not only disrupts the insulating a-SiO_2 layer on the surface of the Si particles, but also improves the interface contact, leading to denser particle accumulation (Fig. S37).

Furthermore, distinct differences in R_{ct} could be observed during the charge/discharge processes (Fig. S38 and Fig. 5g). The initial R_{ct} of Li-In|LPSC|Si@$AlCl_3$ is approximately 71 Ω, significantly lower than that of Li-In|LPSC|Si (470 Ω). During discharge, the formation of highly conductive Li-Si alloys, results in a significant decrease in R_{ct} for both configurations. The R_{ct} values for Li-In|LPSC|Si@$AlCl_3$ and Li-In|LPSC|Si decrease to 18 Ω and 16.5 Ω, respectively, In the charged state, the Li-In|LPSC|Si@$AlCl_3$ maintains a relatively low R_{ct} of 36 Ω, while the Li-In|LPSC|Si exhibits a higher R_{ct} of 443 Ω, as determined through equivalent circuit fitting. DRT analysis indicates that after lithiation/delithiation, the grain boundary and interphase impedance of Li-In|LPSC|Si in the range of 10^{-6}-10^{-4} s increase, contributing to the overall higher R_{ct}. Therefore, the stabilized interface ensures the fast interface charge transfer dynamics.

A comparison of the galvanostatic intermittent titration technique (GITT) curves during discharge reveals the differences in the reaction mechanisms (Fig. S39a). For Li-In|LPSC|Si@$AlCl_3$, the discharge process exhibits a direct single-phase transformation from Si to $Li_{3.75}Si$, bypassing the initial

solid-solution reaction (voltage slope) observed in Li-In|LPSC|Si, which first forms Li_xSi (solid solution) followed by a phase transformation (voltage plateau)[37]. The calculated diffusion coefficients further support the interpretation (Fig. S39b). In the early discharge stage, the phase transition in Li-In|LPSC|Si is kinetically constrained, thereby activating a solid-solution reaction mechanism (manifested by an elevated diffusion coefficient). Remarkably, during the subsequent phase transition, Li-In|LPSC|Si@$AlCl_3$ exhibits a higher average diffusion coefficient (2.96×10^{-10} cm^2 s^{-1}) compared to Li-In|LPSC|Si (2.15×10^{-10} cm^2 s^{-1}), demonstrating enhanced ion transport and reaction kinetics (Fig. 5h).

Benefiting from the improved electro/chemical compatibility and enhanced ion/electron transport kinetics, the Si@$AlCl_3$ negative electrode shows improved reversibility and cyclic stability. In contrast to the rapid capacity decay observed in the pristine Si negative electrode after tens of cycles, the Si@$AlCl_3$ negative electrode maintains a capacity of approximately 700 mAh g^{-1} after 400 cycles at 10.5 A g^{-1}, with its average CE increasing from 99.945% to 99.998% and cumulative CE for 400 cycles increasing from 39.2% to 88.5% (Fig. 6a,b and Fig. S40). Notably, Li-In|LPSC|Si@$AlCl_3$ shows consistently higher average CE than that of Li-In|LPSC|Si across various current rates (Fig. S41). Furthermore, stable cycling performance was maintained even under low external pressure (20 MPa) (Fig. S42). In high-loading Si-based half-cells with capacities exceeding 10 mAh cm^{-2} without adhesives, conductive carbon or additional SE additives, the Li-In|LPSC|Si exhibits significant kinetic limitations and Li plating issues, resulting in an ICE as low as 61.5%, and a two-step reaction mechanism during discharge. In contrast, the Li-In|LPSC|Si@$AlCl_3$ achieves a higher ICE of 78.9% and follows a single-step reaction mechanism (Fig. S43). Furthermore, while the high-loading Li-In|LPSC|Si demonstrates rapid capacity degradation, suffering nearly complete capacity loss after only 80 cycles at 25 °C and 5.1 mA cm^{-2}, with an average CE exceeding 102% indicative of pronounced lithium plating and side reactions[14] (Fig. 6c,d and Fig. S44). In contrast, the Li-In|LPSC|Si@$AlCl_3$ system exhibits improved cycling stability, maintaining 72% capacity retention over 500 cycles at 5.1 mA cm^{-2} with an average CE of 100.06%. Remarkably, at a reduced current density of 1.5 mA cm^{-2}, the system achieved higher capacity utilization (5-6 mAh cm^{-2}) while retaining capacity retention of

88.7% over 50 cycles (Fig. S45).

When paired with a commercial NCM positive electrode, the full cell demonstrates stable cycling performance at 200 mA g^{-1} for 200 cycles with a high capacity retention of 80% and an average CE exceeding 99.95% (Fig. S46). Furthermore, the pre-lithiated Si@$AlCl_3$||NCM full cell[38] achieves an initial charge capacity of 230.8 mAh g^{-1} and a discharge capacity of 199.9 mAh g^{-1}, with a high ICE of 86.6% (Fig. 6e,f).

Furthermore, comparative analysis of modification strategies reveals the advantages of our halide salt-driven surface halogenation engineering. The results reveal that the incorporation of conductive carbon leads to suboptimal negative electrode capacity and $ICE_{negative\ electrode}$ (<85%). Meanwhile, Si-based systems are constrained by the limited active material content, resulting in restricted negative electrode capacity utilization (<2600 mAh g^{-1}). Although structural engineering of Si negative electrodes ensures capacity retention, it still falls short in achieving satisfactory ICE. In contrast, the halide salt-driven modification strategy demonstrates universally enhanced performance in both ICE and capacity utilization, while maintaining stable cycling in full-cell configurations (Fig. 6g, Fig. S47-S48 and Table S6).

In summary, we have developed a halide salts-driven surface halogenation engineering, exemplified by $AlCl_3$, which has been demonstrated to form SA composite layer on Si particles. This composite layer enhances the (electro)chemical compatibility between the Si negative electrode and LPSC electrolyte, ensuring stable interfacial transport kinetics. Simultaneously, it eliminates the intrinsic a-SiO_2 layer on the Si surface, thereby improving the ion/electron transport kinetics of the Si-based negative electrode. Notably, the AlOCl component within the composite layer exhibits high electrochemical stability during cycling, ensuring sustained performance enhancement in subsequent cycles. As a result, this strategy effectively reduces C-Li and K-Li during both the initial and subsequent cycles, ultimately promoting capacity utilization and enhanced reversibility of the Si-based negative electrode.

The modified Si@$AlCl_3$ negative electrode demonstrates remarkable performance in half-cells,

achieving a high ICE of 94.3% and a specific charge capacity of 3324.6 mAh g^{-1} at 25 °C, with an average CE of 99.998% at 10.5 A g^{-1}. Remarkably, even under challenging high-load conditions (>10 mAh cm^{-2}), the system maintains stable cycling for 500 cycles with 72% capacity retention at 5.1 mA cm^{-2} under 25 °C. When paired with NCM positive electrodes, the full-cell delivers stable cycling performance at 200 mA g^{-1} for 200 cycles with a high capacity retention of 80% and an average CE exceeding 99.95%. Combined with a pre-lithiation process, the full-cell achieves an improved ICE of 86.6% for Si-based SSBs. The universal applicability of the halide salt-driven modification strategy has been further validated, offering a promising pathway for developing high-reversibility, high-energy-density Si-based SSBs that meet practical application requirements.

Methods

Synthesis of materials

μSi (Aladdin, 99.9%, 1-3 μm), aluminum chloride ($AlCl_3$, Macklin, 99%), iron chloride ($FeCl_3$, Aladdin, 99.9%), tantalum chloride ($TaCl_5$, Aladdin, 99.8%), bismuth chloride ($BiCl_3$, Aladdin, 99.99%), niobium chloride ($NbCl_5$, Aladdin, 99%), phosphorus pentachloride (PCl_5, Macklin, 98%), magnesium chloride ($MgCl_2$, Aladdin, 99%), antimony trichloride ($SbCl_3$, Aladdin, 99%), zinc chloride ($ZnCl_2$, Macklin, 99%), lithium oxide (Li_2O, Aladdin, 99.99%) and $Na_2SiO_3{\cdot}9H_2O$ (Aladdin, 98%) were purchased as raw materials. Commercial Li_6PS_5Cl (LPSC, Shenzhen Kejing Star Technology CO., LTD.) and Li_3InCl_6 (LIC, Shenzhen Kejing Star Technology CO., LTD.) were used as SE layer. Vapor grown carbon fibre (VGCF, Hefei Kejing, China) and commercial $LiNi_{0.88}Co_{0.09}Mn_{0.03}O_2$ (NCM) were used for the positive electrode.

All synthesis procedures were performed under inert argon atmosphere in a glove box (H_2O<0.01 ppm, O_2<0.01 ppm) using simple thermal treatment.

For μSi@$AlCl_3$, stoichiometric quantities of μSi and $AlCl_3$ were mixed at mass ratios of 90:10, ground manually in an agate mortar for 5 minutes. The resultant mixture was transferred to a sealed glass bottle and subjected to thermal treatment at 180°C on a hotplate for 2 hours, yielding the μSi@$AlCl_3$-10. By adjusting the mass ratios to 95:5 and 85:15 while maintaining identical synthesis conditions, μSi@$AlCl_3$-5 and μSi@$AlCl_3$-15 were prepared respectively.

For other metal chloride modifications (μSi@MCl_x (M= P, Ta, Bi, Fe, Nb, Zn, Mg)), the same procedure

was followed with modified thermal treatment temperatures: 450°C for $ZnCl_2$ and $MgCl_2$, while temperatures were adjusted according to the respective chloride boiling points for others.

$LiTaOCl_4$ was synthesized via solid-state mechanochemical reaction. A stoichiometric mixture of Li_2O and $TaCl_5$ (1 g total) was ball-milled in a ZrO_2 pot (80 mL) with ZrO_2 balls (30 g) at 500 rpm for 24 hours.

Materials characterization

The electrode samples were prepared in a glovebox under an argon atmosphere and transferred to the testing equipment via a sealed sample holder.

Phase structures of the as-prepared materials were investigated by XRD on a Bruker D8 diffractometer (equipped with Cu-Kα radiation) with a scan range of 10-90°. Scanning electron microscopy (SEM, Regulus8230) and Transmission electron microscopy (TEM, JEM-F200) measurements were employed to characterize the morphology, microstructure of samples and phase characteristics of the samples. Energy dispersive spectroscopy (EDS) mappings were carried out to characterize the element distribution. X-ray photoelectron spectroscopy (XPS) was recorded on Axis Supra+ to characterize the valence state and composition of each element in a sample. Gas Chromatography (GC, PE Clarus GC690) was used to analyse the residual Li content of silicon-based negative electrodes. The specific steps include soaking the silica-based negative electrode in absolute ethanol for more than 12 h, during which the residual lithium in the silica-based negative electrode reacts with ethanol to form H_2, and finally the residual lithium content is calculated by detecting the H_2 content[5]. This analytical approach exploits the distinct chemical reactivities of different lithium species: (1) kinetically trapped Li (K-Li) in lithium-silicon alloys reacts vigorously with ethanol to generate H_2, while (2) SEI-consumed Li (C-Li) remains chemically inert under these conditions. The quantification protocol involves three key steps: first, the total irreversible Li (x_{ir}%) is determined from galvanostatic charge-discharge curves as (100% - initial Coulombic efficiency); second, the trapped Li fraction (x_t%) is calculated from the H_2 evolution; finally, the SEI-consumed Li proportion is derived: $x_s=(x_{ir}-x_t)$%.

The Raman analysis was performed with a Raman spectrometer (LabRAM Odyssey) with an excitation wavelength of 532 nm to detect the structural information of the sample. Neutron depth profiling (NDP) was acquired using a cold neutron beam of the China Advanced Research Reactor (CARR)[32]. The working principle is based on the nuclear reaction between ^6Li (natural lithium consists of ^6Li with a relative abundance of 7.5 at. %) and a neutron according to equation:

$$^6Li+n\rightarrow{}^4He\ (2055\ keV) + {}^3H\ (2727\ keV) \quad (1)$$

Depth calibration. The relationship between the detected energy (E) and the depth at which the

charged particles are generated can be established using Stopping and Range of Ions in Matter (SRIM), from which the residual energy of the charged particles generated at different depths of the sample can be calculated. The relationship between the detected energy (E) and their depth (d) of in the 1.5 μm LPSC + d μm Si-based negative electrode is determined to be:

$$d=4.25719\times10^{-7}\times E^2-0.00518\times E+9.17825 \quad (2)$$

All-solid-state ASSBs assembling

All electrodes were made by a traditional slurry-coating way where μSi/Si@$AlCl_3$, poly-(vinylidene fluoride) (PVDF, 99%, Arkema) binder were ground at a mass ratio of 99.7:0.3, and then homogenized in 1-methyl-2-pyrrolidinone (NMP, 99%, Alfa Aesar). The slurry was then bladed on Cu foil (6μm) to render uniform coating, dried for at least 24 h at 60 °C in a vacuum oven, and then punched into circular electrodes with a diameter of 10 mm. The electrode mass loading was around 0.8-1.2 mg cm^{-2}. All SSBs were assembled in an argon-filled glovebox using a mold with an internal diameter of 10 mm. For half-cell configuration, Li-In|LPSC|Si was made with an In foil (thickness: 50 μm; diameter: 10 mm) and a Li foil (thickness: 50 μm; diameter: 8 mm) as negative electrode (mass ratio of In foil and Li foil is 20), 80 mg LPSC as electrolyte layer, and Si electrode as positive electrode layer. The half-cell was pressed at a pressure of about 180 MPa for 5 min to ensure tight interface contact. Li-In|LPSC|Si@$AlCl_3$ was the same as the above assembly process, only the Si electrode needed to be replaced with Si@$AlCl_3$. The stack pressure applied during testing was about 180 MPa as well. For low external pressure testing, the half-cell assembly followed identical fabrication procedures as described above, with the sole modification of reducing the applied pressure to 20 MPa. For high-loading half cells (>9 mAh cm^{-2}), the silicon electrode layer was directly prepared by cold pressing Si or Si@$AlCl_3$ powder at 50 MPa. For full-cell, Si|LPSC|LIC|NCM was made with NCM-based positive electrode composite powder (NCM:LIC:VGCP=70:25:5) as the positive electrode layer, Si electrode as the negative electrode layer, 30 mg LIC as electrolyte layer on the positive side and 50 mg LPSC as electrolyte layer on the negative side. The full-cell was pressed at a pressure of about 400 MPa for 5 min to ensure tight interface contact. The stack pressure applied during testing was about 180 MPa as well. Si@$AlCl_3$|LPSC|LIC|NCM was the same as the above assembly process, only the Si electrode was replaced with Si@$AlCl_3$. The mass loading of NCM positive electrode was about 15-20 mg cm^{-2}. n/p is set between 1.1-1.15, where specific capacity of Si-based negative electrode is 3500 mAh g^{-1} and the specific capacity of NCM is 200 mAh g^{-1}.

Electrochemical tests

LAND CT 2001Abattery testing system was used to conduct galvanostatic measurements of the batteries. Half-cells testing was performed in a voltage window of -0.6-1.4 V (0.02-2.02 V vs. Li^+/Li) at

25 °C and full-cells testing was performed in a voltage window of 2.5-4.3 V at 25 °C. The electrochemical impedance spectroscopy (EIS) was obtained by employing an electrochemical workstation (BioLogic 2) under a potentiostatic mode, with a signal amplitude of 5 mV. The measurements covered a frequency range of 7×10^6 to 10^0 Hz, with 10 data points per decade of frequency. Galvanostatic intermittent titration technique (GITT) measurements to calculate diffusivity were performed at 0.1 C rate with the duration time of each current pulse of 15 minutes and the resting time of 2 h. Direct current (DC) polarization was performed to measure electronic conductivity by obtaining stable current at different constant voltage values for 600 seconds. Cumulative CE is calculated as the product of the CE of each cycle from the first to the *n*th cycle (i.e., cumulative CE = $CE_1 \times CE_2 \times ... \times CE_n$), where CE_n of each cycle is the ratio of discharge capacity to charge capacity. It quantifies the total cumulative lithium loss and long-term reversibility.

Data availability

The authors declare that all the relevant data are available within the paper and its Supplementary Information file or from the corresponding author upon request. Source data are provided with this paper.

References

1 Janek, J. & Zeier, W. G. Challenges in speeding up solid-state battery development. *Nature Energy* **8**, 230-240 (2023). https://doi.org:10.1038/s41560-023-01208-9

2 Janek, J. & Zeier, W. G. A solid future for battery development. *Nature Energy* **1**, 16141 (2016). https://doi.org:10.1038/nenergy.2016.141

3 Huo, H. *et al.* Chemo-mechanical failure mechanisms of the silicon anode in solid-state batteries. *Nature Materials* **23**, 543-551 (2024). https://doi.org:10.1038/s41563-023-01792-x

4 Yan, W. *et al.* Hard-carbon-stabilized Li–Si anodes for high-performance all-solid-state Li-ion batteries. *Nature Energy* **8**, 800-813 (2023). https://doi.org:10.1038/s41560-023-01279-8

5 Tan, D. H. S. *et al.* Carbon-free high-loading silicon anodes enabled by sulfide solid electrolytes. *Science* **373**, 1494-1499 (2021). https://doi.org:10.1126/science.abg7217

6 Ham, S.-Y. *et al.* Overcoming low initial coulombic efficiencies of Si anodes through prelithiation in all-solid-state batteries. *Nature Communications* **15**, 2991 (2024). https://doi.org:10.1038/s41467-024-47352-y

7 Pan, H. *et al.* A solid-state lithium-ion battery with micron-sized silicon anode operating free from external pressure. *Nature Communications* **15**, 2263 (2024). https://doi.org:10.1038/s41467-024-46472-9

8 Cao, D. *et al.* Long-Cycling Sulfide-Based All-Solid-State Batteries Enabled by

Electrochemo-Mechanically Stable Electrodes. *Advanced Materials* **34**, 2200401 (2022). https://doi.org:https://doi.org/10.1002/adma.202200401

9 Zhang, D., Yu, P., Zhang, Y., Zhao, X. & Yu, J. Vertical Graphene Sheet-Encapsulated Silicon Nanoparticles for Anodes of Polymer-Based All-Solid-State Batteries. *ACS Applied Energy Materials* **7**, 726-734 (2024). https://doi.org:10.1021/acsaem.3c02806

10 Yamamoto, M., Terauchi, Y., Sakuda, A. & Takahashi, M. Slurry mixing for fabricating silicon-composite electrodes in all-solid-state batteries with high areal capacity and cycling stability. *Journal of Power Sources* **402**, 506-512 (2018). https://doi.org:https://doi.org/10.1016/j.jpowsour.2018.09.070

11 Cangaz, S. *et al.* Enabling High-Energy Solid-State Batteries with Stable Anode Interphase by the Use of Columnar Silicon Anodes. *Advanced Energy Materials* **10**, 2001320 (2020). https://doi.org:https://doi.org/10.1002/aenm.202001320

12 Huo, H. *et al.* Decoupling the Effects of Interface Chemical Degradation and Mechanical Cracking in Solid-State Batteries with Silicon Electrode. *Advanced Materials* **n/a**, 2415006 (2024). https://doi.org:https://doi.org/10.1002/adma.202415006

13 Huang, Y., Shao, B., Wang, Y. & Han, F. Solid-state silicon anode with extremely high initial coulombic efficiency. *Energy & Environmental Science* **16**, 1569-1580 (2023). https://doi.org:10.1039/D2EE04057C

14 Zhang, Z. *et al.* Silicon-based all-solid-state batteries operating free from external pressure. *Nature Communications* **16**, 1013 (2025). https://doi.org:10.1038/s41467-025-56366-z

15 Li, Y. *et al.* Unveiling the mechanisms into Li-trapping induced (ir)reversible capacity loss for silicon anode. *Energy Storage Materials* **55**, 660-668 (2023). https://doi.org:https://doi.org/10.1016/j.ensm.2022.12.032

16 Cao, D. *et al.* Unveiling the Mechanical and Electrochemical Evolution of Nanosilicon Composite Anodes in Sulfide-Based All-Solid-State Batteries. *Advanced Energy Materials* **13** (2023). https://doi.org:10.1002/aenm.202203969

17 Lee, J. *et al.* Dry Pre-Lithiation for Graphite-Silicon Diffusion-Dependent Electrode for All-Solid-State Battery. *Advanced Energy Materials* **13** (2023). https://doi.org:10.1002/aenm.202300172

18 Ye, L., Lu, Y., Wang, Y., Li, J. & Li, X. Fast cycling of lithium metal in solid-state batteries by constriction-susceptible anode materials. *Nature Materials* **23**, 244-251 (2024). https://doi.org:10.1038/s41563-023-01722-x

19 Iwamura, S. *et al.* Li-Rich Li-Si Alloy As A Lithium-Containing Negative Electrode Material Towards High Energy Lithium-Ion Batteries. *Scientific Reports* **5**, 8085 (2015). https://doi.org:10.1038/srep08085

20 Xiao, J. *et al.* Understanding and applying coulombic efficiency in lithium metal batteries. *Nature Energy* **5**, 561-568 (2020). https://doi.org:10.1038/s41560-020-0648-z

21 Zhao, X., Zhao-Karger, Z., Fichtner, M. & Shen, X. Halide-Based Materials and Chemistry for Rechargeable Batteries. *Angewandte Chemie International Edition* **59**, 5902-5949 (2020). https://doi.org:https://doi.org/10.1002/anie.201902842

22 Su, H. *et al.* A scalable Li-Al-Cl stratified structure for stable all-solid-state lithium metal

batteries. *Nature Communications* **15**, 4202 (2024). https://doi.org:10.1038/s41467-024-48585-7

23 Flores-González, N. *et al.* Mechanochemical Synthesis and Structure of Lithium Tetrahaloaluminates, LiAlX4 (X = Cl, Br, I): A Family of Li-Ion Conducting Ternary Halides. *ACS Materials Letters* **3**, 652-657 (2021). https://doi.org:10.1021/acsmaterialslett.1c00055

24 Cai, M. *et al.* Zincothermic reduction of silica to silicon: make the impossible possible. *Journal of Materials Chemistry A* **9**, 21323-21331 (2021). https://doi.org:10.1039/D1TA06073B

25 Ghita, R. V. *et al.* in *Crystalline Silicon - Properties and Uses* (ed Sukumar Basu) (IntechOpen, 2011).

26 Zhang, S. *et al.* A Universal Self-Propagating Synthesis of Aluminum-Based Oxyhalide Solid-State Electrolytes. *Angew Chem Int Ed Engl* **63**, e202401373 (2024). https://doi.org:10.1002/anie.202401373

27 Je, M. *et al.* Metal-Mediated Chlorine Transfer for Molten Salt-Driven Thermodynamic Change on Silicon Production. *Advanced Science* **12**, 2412239 (2025). https://doi.org:https://doi.org/10.1002/advs.202412239

28 Kaur, A., Chahal, P. & Hogan, T. Selective Fabrication of SiC/Si Diodes by Excimer Laser Under Ambient Conditions. *IEEE Electron Device Letters* **37**, 142-145 (2016). https://doi.org:10.1109/LED.2015.2508479

29 Dai, T. *et al.* Inorganic glass electrolytes with polymer-like viscoelasticity. *Nature Energy* **8**, 1221-1228 (2023). https://doi.org:10.1038/s41560-023-01356-y

30 Duan, H. *et al.* Amorphous AlOCl Compounds Enabling Nanocrystalline LiCl with Abnormally High Ionic Conductivity. *Journal of the American Chemical Society* **146**, 29335-29343 (2024). https://doi.org:10.1021/jacs.4c06498

31 Yu, J. *et al.* A low temperature MgH2-AlCl3-SiO2 system to synthesize nano-silicon for high-performance Li-ion batteries. *Chemical Engineering Journal* **406**, 126805 (2021). https://doi.org:https://doi.org/10.1016/j.cej.2020.126805

32 Han, F. *et al.* High electronic conductivity as the origin of lithium dendrite formation within solid electrolytes. *Nature Energy* **4**, 187-196 (2019). https://doi.org:10.1038/s41560-018-0312-z

33 Yang, Z. *et al.* Surface passivated LixSi with improved storage stability as a prelithiation reagent in anodes. *Electrochemistry Communications* **138**, 107272 (2022). https://doi.org:https://doi.org/10.1016/j.elecom.2022.107272

34 Fang, R. *et al.* Reaction Mechanism Optimization of Solid-State Li–S Batteries with a PEO-Based Electrolyte. *Advanced Functional Materials* **31**, 2001812 (2021). https://doi.org:https://doi.org/10.1002/adfm.202001812

35 Wood, K. N. *et al.* Operando X-ray photoelectron spectroscopy of solid electrolyte interphase formation and evolution in Li2S-P2S5 solid-state electrolytes. *Nature Communications* **9**, 2490 (2018). https://doi.org:10.1038/s41467-018-04762-z

36 Lu, Y., Zhao, C.-Z., Huang, J.-Q. & Zhang, Q. The timescale identification decoupling

complicated kinetic processes in lithium batteries. *Joule* **6**, 1172-1198 (2022). https://doi.org:https://doi.org/10.1016/j.joule.2022.05.005

37 Jiang, Y., Offer, G., Jiang, J., Marinescu, M. & Wang, H. Voltage Hysteresis Model for Silicon Electrodes for Lithium Ion Batteries, Including Multi-Step Phase Transformations, Crystallization and Amorphization. *Journal of The Electrochemical Society* **167**, 130533 (2020). https://doi.org:10.1149/1945-7111/abbbba

38 Jin, L. *et al.* Pre-Lithiation Strategies for Next-Generation Practical Lithium-Ion Batteries. *Advanced Science* **8**, 2005031 (2021). https://doi.org:https://doi.org/10.1002/advs.202005031

Acknowledgements

This work was supported by the National Natural Science Foundation of China (22075268, 22409173, 22472079, W2441017), the Key R&D Program of Zhejiang (2024SSYS0050), the Zhejiang Provincial Natural Science Foundation of China (LQ24B030015), and Zhejiang Provincial Postdoctoral Science Foundation (ZJ2024026).

Author Contributions

H. L. conceived and designed the experimental work and prepared the manuscript. Y. L. revised the Figures. G. H. and Y. L. provided technical guidance for solid-state battery assembly processes. C. X. and L. Z. performed NDP characterization. H. H. revised the manuscript. H. Z. supplemented the interfacial reaction calculation. W. X. and N. L. supervised the overall project and revised the manuscript. All authors have given approval to the final version of the manuscript.

Competing Interests

The authors declare no competing interests.

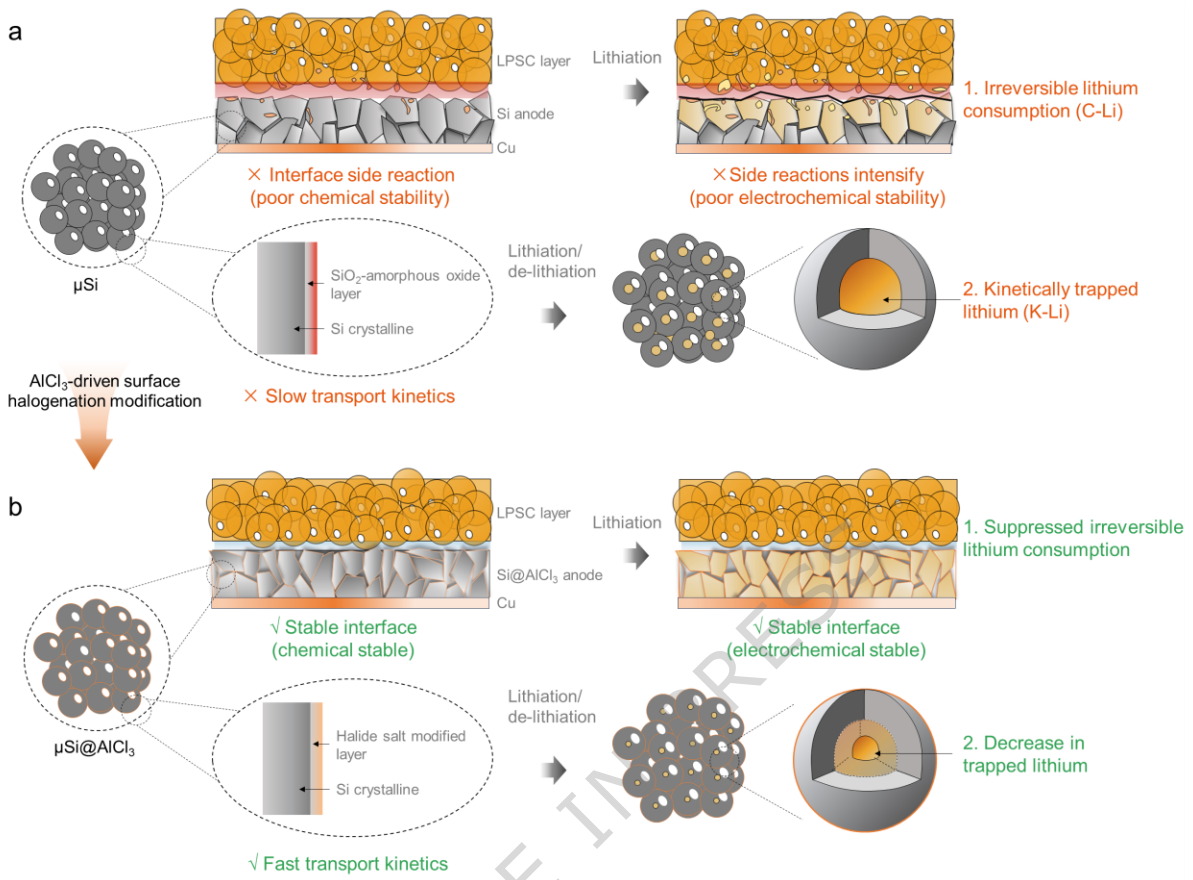

Figure 1. Mitigation mechanism of irreversible lithium loss via surface halogenation strategy. Schematic illustration of the sources of irreversible Li loss in Si-based negative electrodes within SSB configurations, through comparative analysis of **(a)** pristine Si and **(b)** Si@$AlCl_3$ negative electrodes. The schematic diagram reveals that irreversible Li predominantly originates from two distinct mechanisms: Li consumption for SEI formation (C-Li) and kinetically trapped Li (K-Li).

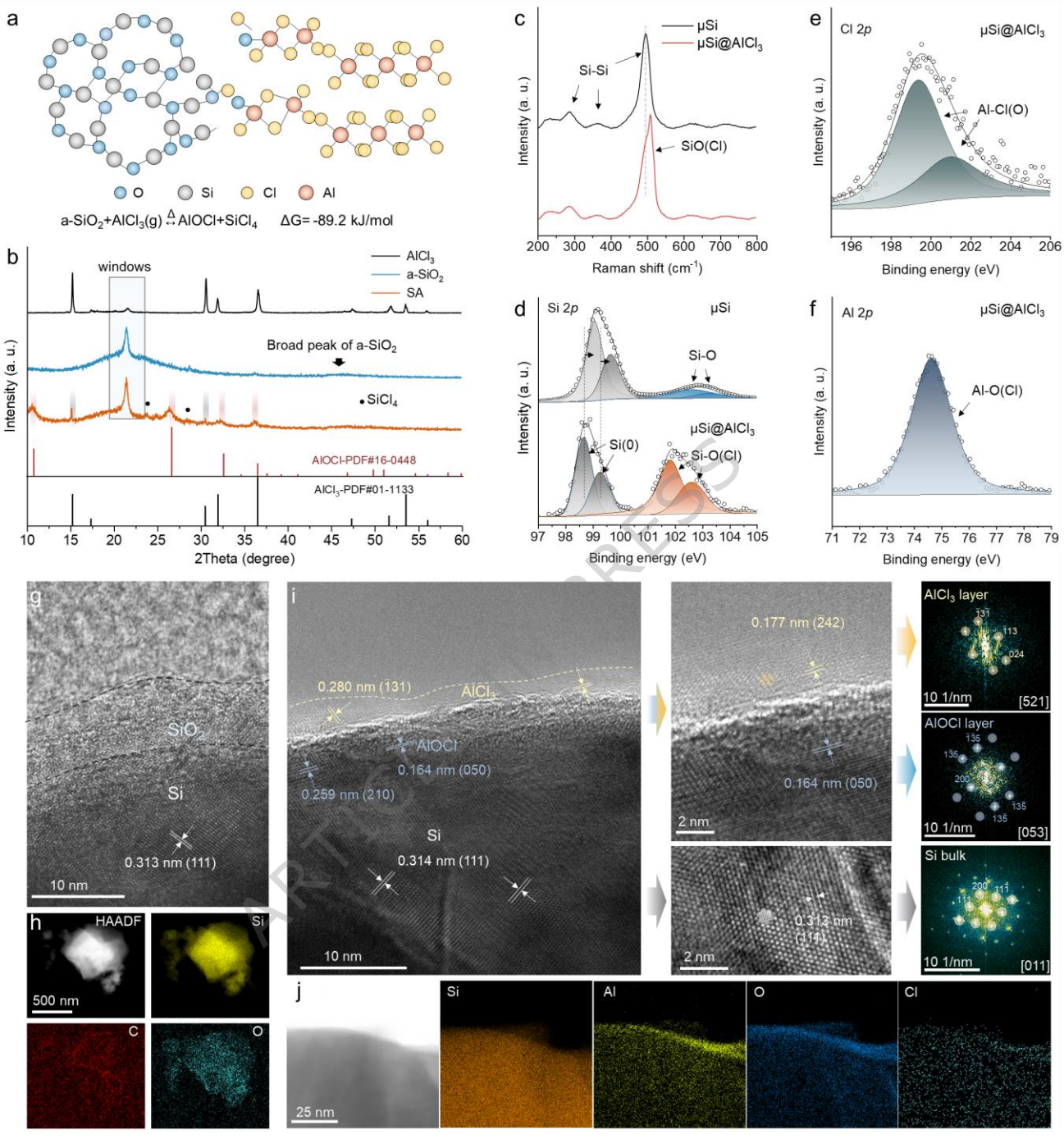

Figure 2. Validation experiments of the halogenation reaction and structural/elemental characterizations of the Si@AlCl$_3$. (**a**) Schematic diagram and reaction equation for the inferred halogenation reaction between a-SiO$_2$ and AlCl$_3$; (**b**) XRD patterns of a-SiO$_2$, AlCl$_3$, SA; (**c**) Raman spectra of Si and Si@AlCl$_3$; (**d**) XPS Si 2*p* spectra of Si and Si@AlCl$_3$, along with XPS (**e**) Cl 2*p* and (**f**) Al 2*p* spectra of Si@AlCl$_3$; (**g**) HRTEM image and (**h**) 2D EDS mapping of the Si surface; (**i**) HRTEM image and (**j**) 2D EDS mapping of the Si@AlCl$_3$ particle surface with corresponding FFT results.

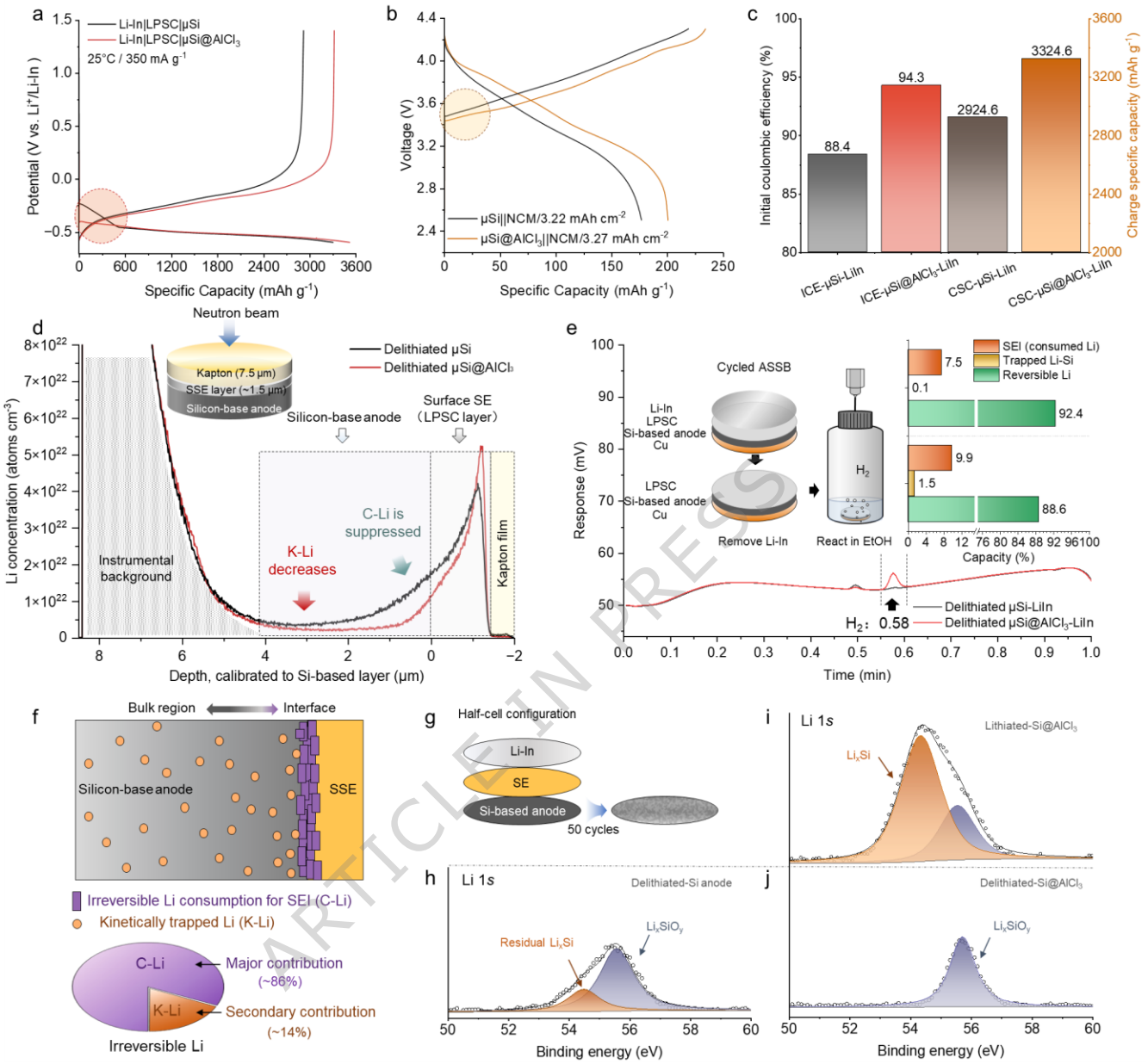

Figure 3. Study of irreversible lithium loss. (**a**) Galvanostatic charge-discharge (GCD) profiles of Li-In|LPSC|Si@$AlCl_3$ and Li-In|LPSC|Si; (**b**) GCD profiles of Si@$AlCl_3$||NCM and Si||NCM (LIC means Li_3InCl_6); (**c**) Comparison results of the first CE and the charge specific capacity (CSC) of the Si active material corresponding to the Si and Si@$AlCl_3$ negative electrodes; (**d**) The NDP results on the negative side of delithiated Li-In|LPSC|Si@$AlCl_3$ and Li-In|LPSC|Si; (**e**) Schematic diagram of GC sample preparation, the test results and the distribution of irreversible Li (detailed discussions regarding the quantitative proportions of C-Li and K-Li are provided in the **Supplementary Information**); (**f**) Schematic diagram of the distribution and proportion of irreversible Li. (**g**) Schematic diagram for the preparation of the Si-based negative electrodes after multiple cycles; XPS analysis of (**h**) Li 1*s* of the delithiated-μSi negative electrode after 50 cycles; XPS analysis of Li 1*s* spectra for the (**i**) lithiated-μSi@$AlCl_3$ and (**j**) delithiated-μSi@$AlCl_3$ electrode after 50 cycles. Galvanostatic cycling of the above cells were at a current density of 3500 mA g^{-1} and 25˚C. The lithiated state refers to the fully discharged state at -0.6 V (vs. Li^+/Li-In), while the delithiated state denotes the fully charged state at 1.4 V (vs. Li^+/Li-In).

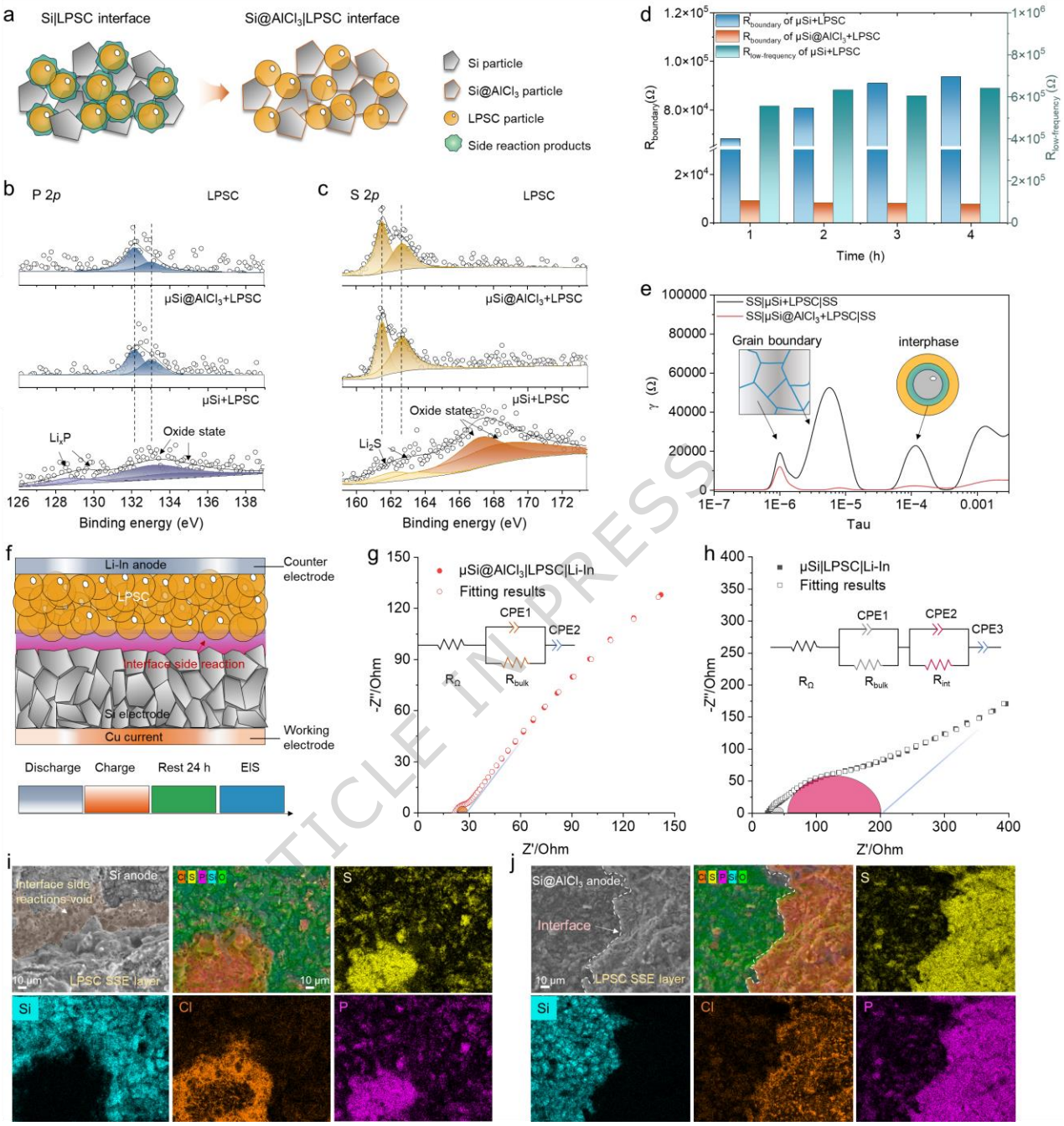

Figure 4. Electrochemical/chemical compatibility of Si-based negative electrode with LPSC. (**a**) Schematic illustration of the preparation process for the mixture used in the chemical compatibility tests between Si or Si@$AlCl_3$ and the LPSC SE; (**b**) XPS P 2*p* spectra and (**c**) XPS S 2*p* spectra of LPSC, Si+LPSC and Si@$AlCl_3$+LPSC; (**d**) Impedance spectra statistics of Si+LPSC and Si@$AlCl_3$+LPSC at different time intervals; (**e**) Distribution of relaxation times (DRT) analysis for Si+LPSC and Si@$AlCl_3$+LPSC; (**f**) Schematic diagram of the structure of the Li-In|LPSC|Si half-cell, and the procedure steps of charge-discharge are given. (**g**) EIS of Li-In|LPSC|Si and (**h**) Li-In|LPSC|Si@$AlCl_3$ after one charge and discharge and its fitting results; (**i**) The SEM images at the interface between the Si negative electrode and the SE layer of Li-In|LPSC|Si after 20 cycles showed significant interfacial voids and side reaction products. (**j**) SEM image of Li-In|LPSC|Si@$AlCl_3$ at the interface between the Si@$AlCl_3$ negative electrode and SE layer after 20 cycles. Galvanostatic cycling of the above cells were at a current density of 3500 mA g^{-1} and 25˚C.

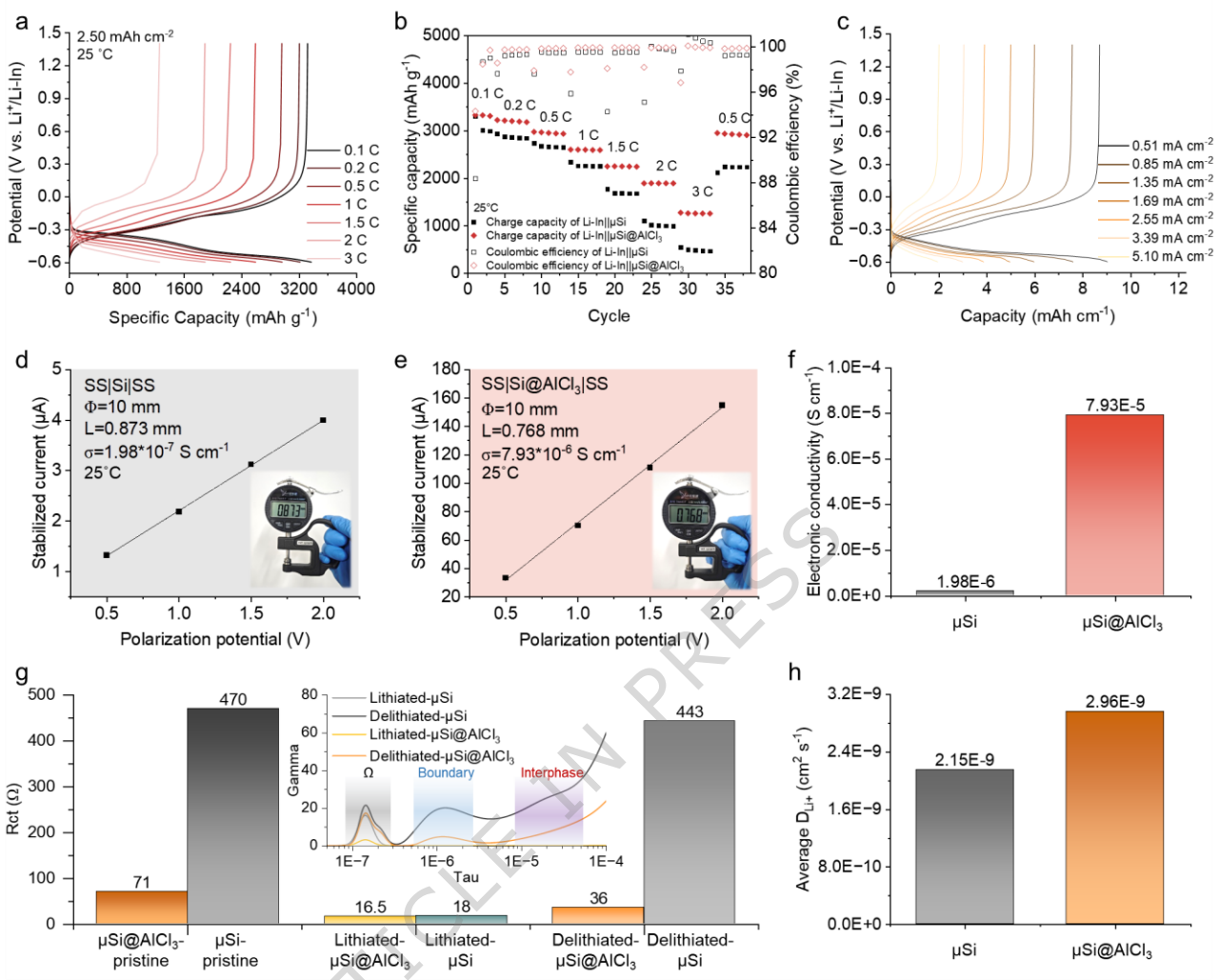

Figure 5. Rate performance and charge transport kinetics. (**a**) GCD profiles of Li-In|LPSC|Si@$AlCl_3$ at different C-rates (1C=3500 mA g^{-1}); (**b**) Rate performance of Li-In|LPSC|Si@$AlCl_3$ and Li-In|LPSC|Si; (**c**) Rate performance of Li-In|LPSC|Si@$AlCl_3$ half-cells under high loading (>9 mAh cm^{-2}) and 25 °C; The electronic conductivity of (**d**) Si and (**e**) Si@$AlCl_3$ obtained by fitting the results; (**f**) Compared with the electronic conductivity, the increase is significantly more than 40 times. The R_{ct} statistical results and DRT analysis for (**g**) Li-In|LPSC|Si@$AlCl_3$ and Li-In|LPSC|Si in different electrochemical states. (**h**) Statistical results of the average diffusion coefficient of the correspondingphase transition process. The test temperature of the above cells was 25˚C.

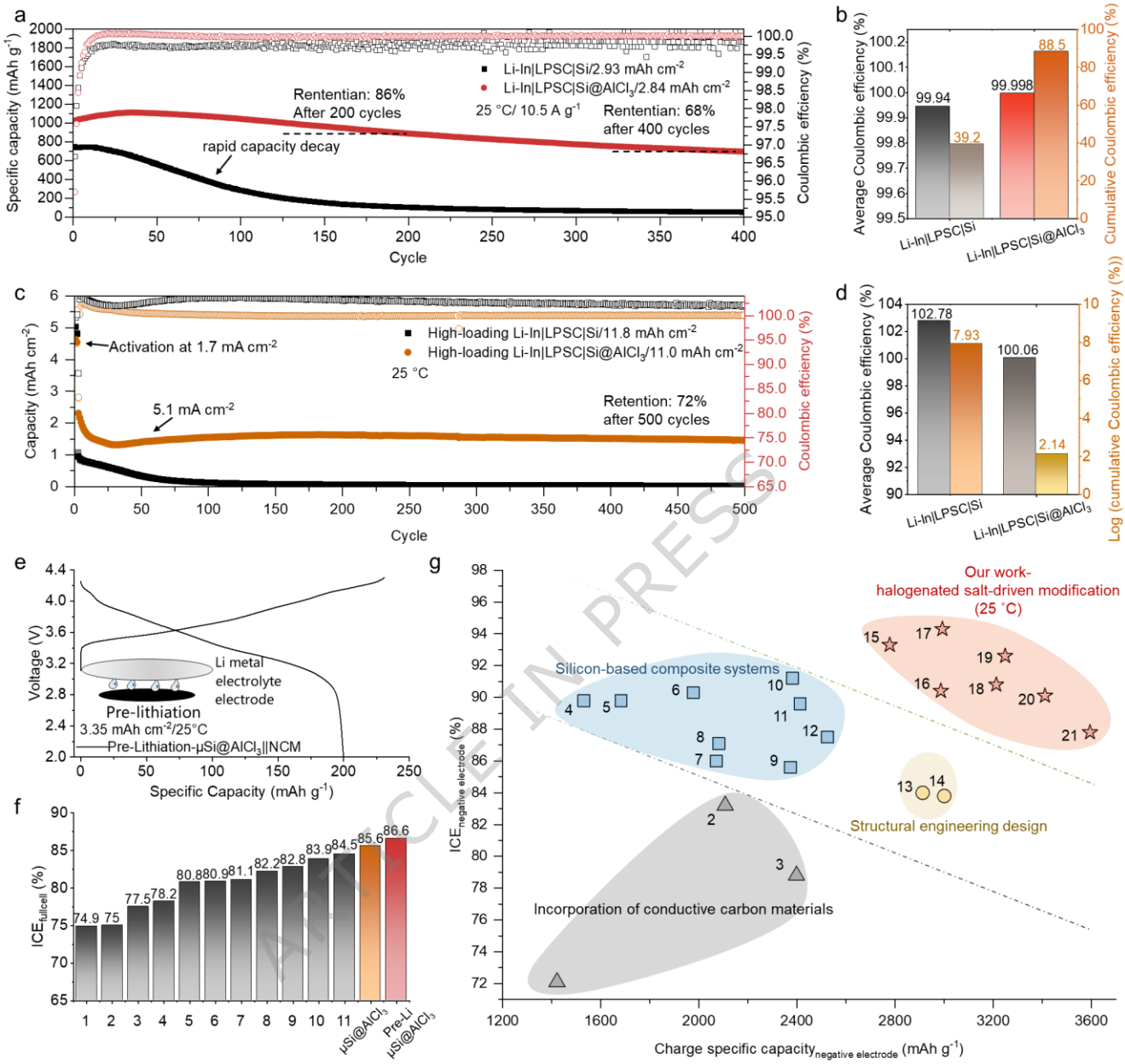

Figure 6. Electrochemical performance of Si-based SSBs with halide salt-driven modification strategy. Comparison of (a) cycling performance of Li-In|LPSC|Si@$AlCl_3$ and Li-In|LPSC|Si at 25 °C and 10.5 A g^{-1}, and (b) the corresponding average CE and Cumulative CE. Comparison of (c) cycling performance of high-loading Li-In|LPSC|Si@$AlCl_3$ and high-loading Li-In|LPSC|Si (>10 mAh cm^{-2}, see **Figure S43**) at 25 °C and 5.1 mA cm^{-2}, and (d) the corresponding average CE and cumulative CE. (e) GCD profiles of Si@$AlCl_3$||NCM after pre-lithiation at 25 °C. (f) ICE statistics of Si-based SSBs with NCM positive electrode (see **Table S3**). (g) Comprehensive performance statistics of Si@MCl_x with previously reported results of Si-based negative electrodes in SSBs (M=Al, Ta, Bi, P, Fe, Nb, Sb, the corresponding GCD profiles are presented in **Figure S47-S48**; statistical information, including charge specific capacity$_{negative\ electrode}$, ICE$_{negative\ electrode}$ and the references corresponding to the numbered entries, is summarized in **Table S6**).

Editor's Summary

Silicon negative electrodes in solid-state batteries exhibit poor reversibility. Here, the authors demonstrate surface halogenation engineering that suppresses irreversible lithium loss, achieving 94.3% initial Coulombic efficiency and 72% capacity retention over 500 cycles at 25°C.

Peer review information: *Nature Communications* thanks Daxian Cao, Gemeng Liang and Jongwoo Lim for their contribution to the peer review of this work. A peer review file is available.